Ammar Trakić
Teaching Assistant
Vehicle Engineering Department
University of Sarajevo
Faculty of Mechanical Engineering
Sarajevo 71 000
Bosnia and Herzegovina

Mirsad Trobradović
Associate Professor
Vehicle Engineering Department
University of Sarajevo
Faculty of Mechanical Engineering
Sarajevo 71 000
Bosnia and Herzegovina

Dževad Bibić
Full Professor – Head of Department
Vehicle Engineering Department
University of Sarajevo
Faculty of Mechanical Engineering
Sarajevo 71 000
Bosnia and Herzegovina

Ejub Džaferović
Full Professor – Head of Department
Department of Energy, Process Engineering and Environmental Engineering
University of Sarajevo
Faculty of Mechanical Engineering
Sarajevo 71 000
Bosnia and Herzegovina

Windbreak and Viaduct Effects on Vehicle Aerodynamics: A CFD Study

This study presents a numerical analysis of the airflow around a passenger vehicle (DrivAer model in the Notchback configuration) travelling across a viaduct, with the aim of investigating the influence of bridge protection elements on the vehicle's aerodynamic characteristics. CFD simulations were conducted in STAR-CCM+ using the RANS approach coupled with the k-ω SST turbulence model. Four geometric configurations were analysed: open flow without any protection, viaduct with a guardrail, viaduct with a solid windbreak, and viaduct with a porous windbreak. Each configuration was simulated under two flow scenarios, with and without a crosswind component. The CFD model was validated against experimental data obtained from the Technical University of Munich (TUM) wind tunnel, showing satisfactory agreement in the drag and pressure coefficients. The results indicate that the solid windbreaks increase side forces and rolling moments, whereas the porous windbreaks significantly reduce turbulent effects and improves aerodynamic stability. The analysis of the Q - criterion field and turbulent kinetic energy confirms that the porous barrier narrows the wake region and diminishes vortex structures behind the vehicle. It was further established that for passenger vehicles, a well-designed guardrail can achieve comparable or even superior effects to complex windbreak in terms of optimizing aerodynamic loads on the vehicle.

Keywords: *Vehicle Aerodynamics, CFD, k-ω SST, Viaduct, Windbreaks, Aerodynamics Coefficients.*

1. INTRODUCTION

The aerodynamic characteristics of a vehicle represent one of the key factors influencing its energy efficiency, stability, and driving safety. During the design process, vehicle body shapes are optimized to reduce aerodynamic drag, which directly affects fuel consumption [1] or, in the case of electric vehicles, overall energy efficiency [2]. Aerodynamic optimization also contributes to noise reduction [3] and enhances stability under various driving conditions [4]. Although vehicle aerodynamics have been extensively studied under standardized conditions, real-world driving environments often differ significantly from those replicated in wind tunnels [5, 6]. Particularly challenging are environments such as bridges, viaducts, and tunnels, where the surrounding infrastructure disturbs the already unsteady airflow caused by variable winds [7, 8]. The non-stationary nature of airflow in these areas arises from the influence of topography and terrain features, which lead to flow separation, deflection, and the formation of vortices and gusts. These effects are especially pronounced on viaducts, which are often constructed in transitional regions between hilly or mountainous areas, where aerodynamic disturbances tend to be most intense [9].

For heavy vehicles, it has been proven that driving on elevated structures leads to significant changes in aerodynamic coefficients, accompanied by increases in side force and roll moment, which in turn raises the risk of destabilization under the influence of crosswinds [10]. Conversely, some studies [11] indicate that bridge pylons can act protectively, reducing side forces as the vehicle approaches their influence zone. However, once the vehicle passes through the turbulent wake behind the pylon, a sudden increase in yaw or rolling moment often occurs due to the large pressure difference between the front and lateral sides of the vehicle. In addition to bridge pylons, guardrails also have an important influence on vehicle aerodynamic behaviour. Their design can considerably alter the characteristics of the airflow and, consequently, the aerodynamic forces acting on the vehicle. Non-porous barriers contribute to smoother flow and greater stability, but they may also cause the "trapping" of air between the barriers, generating a vortex field that negatively affects vehicle stability [12]. Barrier porosity influences the load balance between the bridge and the vehicle. Higher porosity reduces the load on the bridge structure but increases the forces acting on the vehicle, and vice versa [13].

Besides porosity, barrier height is also an important design parameter. Research [14] has shown that increasing height does not lead to a proportional reduction in side forces, meaning that an optimal height must be determined to ensure aerodynamic efficiency without unnecessarily increasing the structure's mass and load. These studies also highlight that the vehicle's lateral position within the traffic lane significantly affects the distribution of aerodynamic forces and moments. This

Received: January 2026, Accepted: April 2026
Correspondence to: Mr Ammar Trakić, Faculty of Mechanical Engineering, Vilsonovo šetalište 9, 71000 Sarajevo, Bosnia and Herzegovina
E-mail: trakic@mef.unsa.ba
doi: 10.5937/fme2602338T

effect is particularly pronounced for high-profile vehicles, where even small shifts in lane position can considerably change side forces and roll moments [7]. It has been established that the side force coefficient (C_S) increases notably from the most exposed to the most sheltered lane, while the lift (C_L) and yaw moment (C_Y) coefficients show a mild increase, and the roll moment coefficient (C_R) tends to decrease.

Previous research has predominantly focused on heavy vehicles, while passenger vehicles, despite their practical importance, have received comparatively less attention. Moreover, many earlier studies were based on simplified geometric models that do not accurately reflect the real complexity of modern vehicle body shapes. In this study, the DrivAer model [15] was employed, representing an optimal compromise between the realistic geometric complexity of passenger vehicle bodies and the simplicity of idealized models such as the Ahmed Body [16, 17]. Consequently, these simplified approaches often fail to predict the nuanced aerodynamic responses caused by the turbulent interference between the vehicle and localized infrastructure. This study bridges that gap by providing an analysis of how realistic passenger car geometries interact with windbreaks, offering a level of detail that is currently lacking in the available literature.

The primary objective of this research is the quantitative comparison of aerodynamic coefficients obtained through CFD simulations for two distinct scenarios: a vehicle in open-air flow (without environmental interference) and a vehicle on a bridge with various guardrail configurations. In this study, the Reynolds-Averaged Navier-Stokes (RANS) approach with the k-ω SST turbulence model was employed. Although RANS provides time-averaged values and statistically models turbulent structures, it remains a reliable method for engineering assessments of vehicle aerodynamic characteristics. Its primary advantage lies in computational efficiency, as it yields satisfactory predictions of integral aerodynamic coefficients on relatively coarser meshes compared to high-fidelity methods. In contrast, Hybrid and Large Eddy Simulation (LES) models resolve vortex structures more realistically but necessitate significantly finer meshes. Meshes that are adequate for a RANS approach are often too coarse for hybrid or LES models, which may lead to less accurate aerodynamic predictions than the RANS approach [17].

Aforementioned scenarios were examined under two flow conditions, one with zero yaw angle and another with an added crosswind component to assess the environmental influence on the aerodynamic behaviour of the vehicle. The results enable a detailed qualification of the flow characteristics and precise identification of the differences in aerodynamic coefficients between idealized and realistic conditions. This emphasizes the importance of incorporating realistic environmental effects into numerical analyses, with similar implications for wind tunnel investigations. Consequently, the study highlights the necessity of developing new testing methodologies that more accurately replicate real driving conditions, which is essential for further optimization of vehicle shapes and achieving superior aerodynamic performance.

2. MATERIALS AND METHODS

2.1 Geometry of vehicle and bridge

In this study, the DrivAer model [15] in the Notchback configuration was used, featuring a smooth underbody, side mirrors, open rims, and realistic tires (designated as N_S_wM_wW). The DrivAer model was developed through a joint collaboration between the Technical University of Munich (TUM), Audi AG, and BMW Group, with the objective of providing the scientific community with a reference CAD vehicle model whose geometry accurately represents the aerodynamic properties of modern passenger vehicles. The model's geometry is derived from the characteristics of the Audi A4 and BMW 3 Series, resulting in a generic vehicle representation in terms of overall body shape and proportions. The DrivAer model was created to ensure comparability of numerical simulation results, as earlier CFD validation efforts relied on simplified geometries such as the Ahmed Body [16] and Davis model [19].

Although such models are useful for understanding the fundamental flow phenomena around vehicles, they lack the geometric and aerodynamic complexity characteristic of real passenger vehicle. Due to its open-access nature and the availability of experimental wind tunnel data, the DrivAer model has become the benchmark geometry for CFD validation in vehicle aerodynamics. It is designed in a modular manner, allowing modifications to the rear section of the body, thereby enabling three configurations: Notchback, Fastback, and Estateback. In this research, the Notchback configuration was employed at full scale (1:1), with its principal dimensions illustrated in Figure 1. This configuration was selected for its balanced representation of aerodynamic complexity and typical mid-size passenger vehicle geometry, making it particularly suitable for studying the influence of environmental conditions on vehicle aerodynamic characteristics.

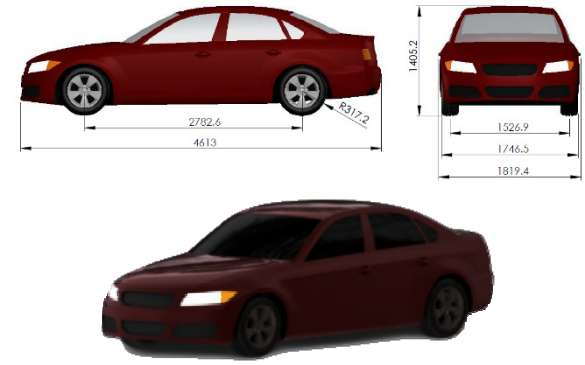

Figure 1. DrivAer model in Notchback configuration

As part of this research, CFD simulations were conducted to analyse the airflow around the DrivAer model under four distinct environmental configurations, with the objective of quantifying the influence of infrastructure and crosswind effects on the vehicle's aerodynamic coefficients. The first case represents the reference flow configuration, in which the vehicle was placed on a moving ground, while the boundaries of the computational domain were positioned sufficiently far from the vehicle to eliminate any boundary-induced

flow interference. This setup corresponds to an idealized wind tunnel condition with optimal blockage ratios and serves as a baseline case for comparison and validation purposes. The second case involves the simulation of airflow over a viaduct segment representative of a typi–cal highway bridge section, featuring only a "New Jersey" type safety barrier along its edges. The third case maintains the same viaduct geometry but includes the addition of a solid windbreak panel mounted above the safety barrier. The fourth case incorporates a porous windbreak, designed with regularly spaced rectangular openings that allow partial air passage, thus modifying the wake dynamics and pressure distribution around the vehicle. All four configurations are illustrated in Figure 2 (a-d, respectively). For each of the four previously defined configurations, two airflow scenarios were si–mulated. In the first scenario, the airflow was directed along the longitudinal axis of the vehicle, with a free-stream velocity of $U = 42\ m/s$, corresponding to a zero-yaw angle ($\beta = 0°$). In the second scenario, a crosswind component of $W = 10\ m/s$ was introduced, resulting in a resultant airflow velocity of $V = 43.2\ m/s$ and an effective yaw angle of approximately $\beta \approx 13.4°$, as illustrated in Figure 3.

In Cases 2, 3, and 4, the vehicle was positioned on the viaduct sur-face within the first driving lane, i.e. the lane most exposed to the crosswind (Figure 4). The primary distinction between these three cases lies in the geometry of the protective barrier. Specifically, in the design and construction of the applied windbreak on the analysed viaduct segment.

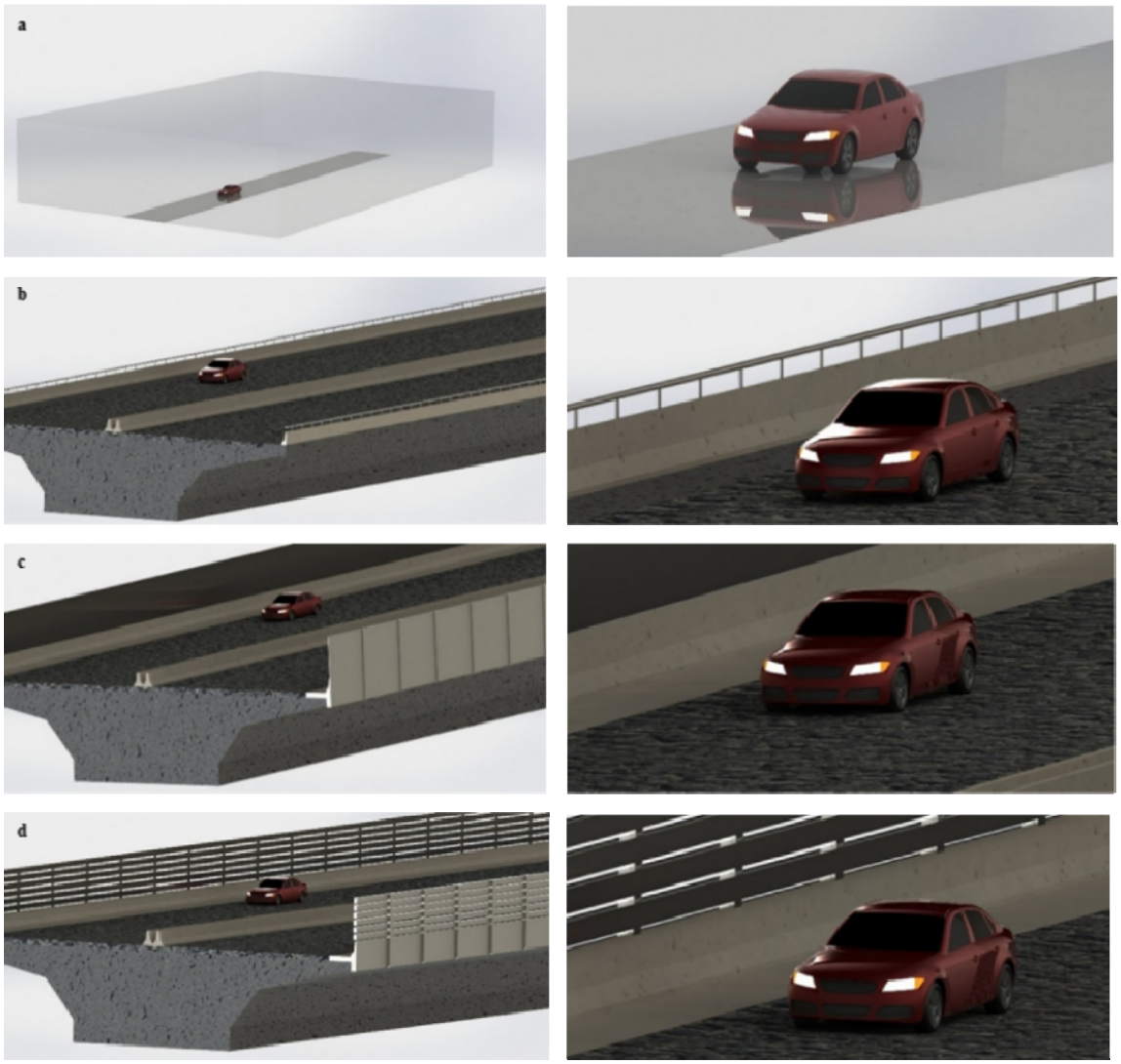

Figure 2. Four simulation cases: a) *Case 1*, b) *Case 2*, c) *Case 3* and d) *Case 4*

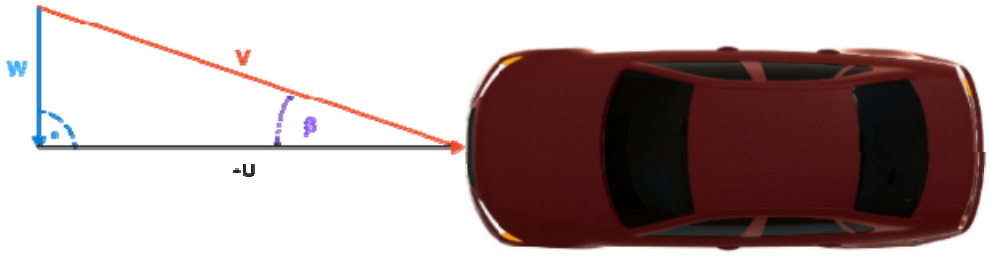

Figure 3. Components of free stream velocity

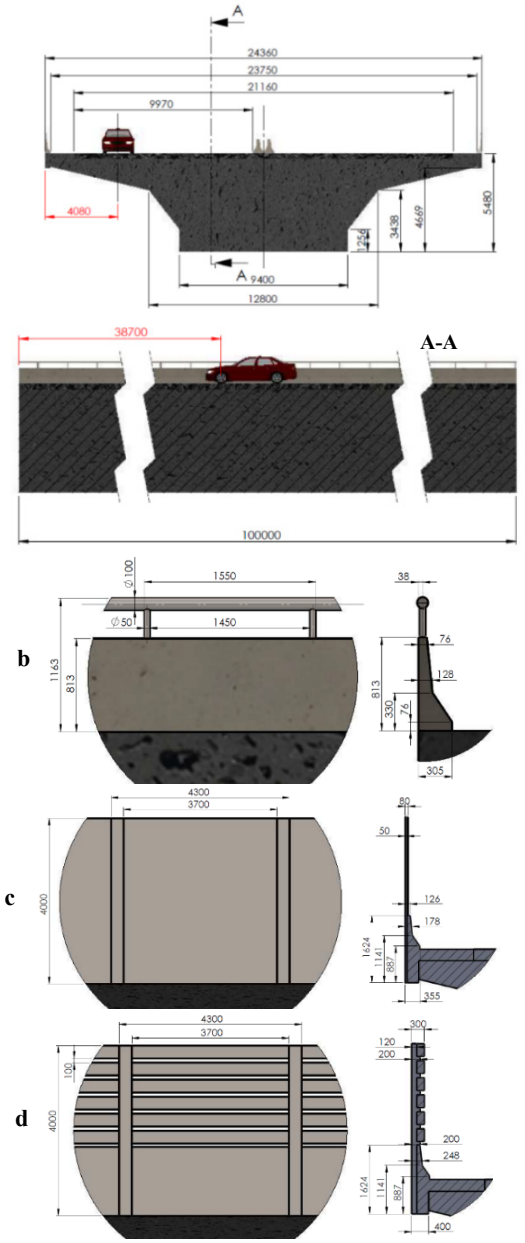

Figure 4. Dimensions of viaduct and windbreaks: b) *Case 2*, c) Case *3* and d) *Case 4*

2.2 Boundary conditions and mesh

For all simulated cases, a three-dimensional Cartesian coordinate system (x, y, z) was adopted. The x-axis is oriented in the longitudinal direction of the vehicle but opposite to the direction of travel. The y-axis is horizontal and perpendicular to the x-axis, representing the lateral direction, while the z-axis is vertical and oriented opposite to the direction of gravitational force. The origin of the global coordinate system is positioned in the plane of the front axle, precisely at its mid-point.

Accordingly, the computational domain dimensions for Case 1 were defined to form a rectangular paral–lelepiped. The inlet boundary, at which free-stream flow conditions were prescribed via the air velocity vector, was located at a distance of $x = -6.5L$ (where L is the total vehicle length). The outlet boundary was placed at $x = 15L$, while the side boundaries were set at $y = \pm 22W$ (where W denotes the vehicle width). The upper boundary was set at a position of $z = 18H$, where H represents the vehicle height. On the side, upper, and outlet boundaries, a pressure outlet condition was applied, allowing the airflow to freely exit the compu–tational domain without artificial reflections or back-flow. This approach is a crucial factor in accurately capturing the complex turbulent structures in the wake region and around the protective barriers.

The bottom boundary of the domain was positioned at $z = -317$ *mm*, such that the wheels were partially embedded into the ground plane, ensuring a physically realistic contact and proper representation of the boundary layer interaction between the vehicle and the road surface. This setup enables more accurate near-ground flow prediction and a realistic reproduction of aerodynamic phenomena occurring in the underbody region. Within a 7 m wide zone surrounding the vehicle (at bottom plane of domain), a wall function (no-slip) was used, with the ground velocity set equal to the vehicle velocity U (see Figure 2a).

The vehicle body surfaces were defined as wall function with no-slip (Body), while the wheels were modelled as rotating walls with an angular velocity of 132 rad/s. For Cases 2, 3, and 4, the computational domain maintained the same horizontal dimensions, while the lower boundary was shifted to $z = -8.6H$ to include the volume beneath the viaduct structure. In these cases, the moving ground condition was applied only to the asphalt deck, whereas all other surfaces were modelled as stationary walls functions (no-slip), as illustrated in Figure 5. The computational mesh was initially designed with the aim of maintaining y^+ values within the range of 20 to 300 across the majority of the surfaces. However, due to the high geometric comple–xity of the vehicle and the viaduct, certain regions exhi–bit y^+ values lower than 1, necessitating a wall treatment capable of handling both low and high y^+ conditions. To address this, the Blended Wall Function (*BWF*) within STAR-CCM+ was utilized, as it accounts for all three sublayers (viscous, buffer, and logarithmic) and pro–vides a continuous transition based on the local y^+ value. This approach is particularly effective for non-uniform distributions, ensuring that the need for extreme mesh refinement near the walls was avoided while mainta–ining satisfactory accuracy and computational efficiency.

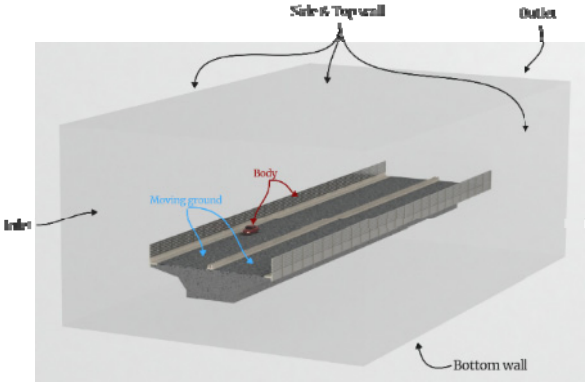

Figure 5. Domain and boundary conditions: *Case 2*, *3* and *4*

The air characteristics, along with the turbulence intensity and turbulent length scale used in all simula–tions, are presented in Table 1. The inlet turbulence

intensity (I) was set to 0.2% with a corresponding turbulent length scale, matching the experimental conditions of the wind tunnel used for validation [15, 20]. While real-world operating conditions often involve significantly higher atmospheric turbulence intensities (frequently exceeding 15% depending on wind conditions and terrain) [21], this study specifically focuses on the turbulence induced by the immediate infrastructure. The presence of the viaduct and windbreak directly modifies the local flow field and turbulence levels surrounding the vehicle. It should be noted that at lower flow velocities, the influence of the Reynolds number on the separation zones becomes more pronounced, although the prescribed turbulence parameters remain consistent with the validated experimental setup to ensure comparative accuracy.

The discretization of the computational domain was carried out using a hexahedral volume. In the region immediately adjacent to the vehicle surface and protective barriers, prismatic layers were applied to ensure accurate modelling of velocity and turbulent viscosity gradients near the walls. A total of 10 prism layers were generated, with a stretching factor of 1.2, enabling a smooth transition towards the free-stream region. The main volume mesh was generated using a combination of the trimmer and surface wrapper tools. The surface wrapper was used to automatically close small surface imperfections, while the trimmer created a semi-structured mesh with hexahedral topology, which enhances solution stability and reduces numerical diffusion in regions with strong velocity gradients.

Table 1. Vehicle and air characteristics

Scenario	1	2
Scale	1:1	1:1
Frontal area	2.16 m²	2.16 m²
Reference length	4613 mm	4613 mm
Vehicle wheelbase	2783 mm	2783 mm
Reynolds number	1.287×10^7	1.323×10^7
Free stream velocity	U= 42 m/s; W = 0 m/s	U= 42 m/s; W = 10 m/s
Density of air	1.204 kg/m^3	1.204 kg/m^3
Referent pressure	101325 Pa	101325 Pa
Dynamic viscosity	1.813×10^{-5} Pa s	1.813×10^{-5} Pa s
Turbulence intensity	0.2 %	0.2 %
Turbulent length scale	5 mm	5 mm

The base size of the mesh elements was set to 48 mm, with local refinements applied around the vehicle in areas where flow separation and recirculation were expected (Figure 6a). Additional refinements were introduced around the guardrails and windbreaks in the viaduct con-figurations (Figure 6b). Mesh refinement followed the principle of percentage of base size, with values varying from 10 % to 90 %, depending on the location and aerodynamic importance of each region. The total number of cells for Case 1 was approximately 18.2 million, while for Cases 2, 3, and 4, the count ranged from 32 to 33 million, depending on the geometry of the guardrails or windbreak. To verify the adequacy of the mesh resolution, a validation procedure was conducted by comparing the CFD results with experimental data available in the literature [20].

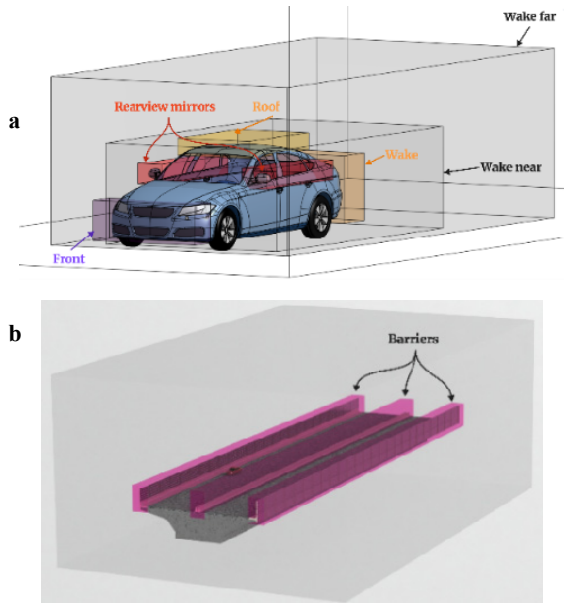

Figure 6. Refinement zone in computational domain

2.3 Equations and solver

The airflow around the vehicle in all analysed configurations was modelled as three-dimensional, unsteady, incompressible turbulent flow, governed by the fundamental equations of fluid mechanics. This set of governing equations includes the continuity equation, the Navier-Stokes momentum equations, and, when necessary, the energy conservation equation. These equations originate from the classical work of Navier and Stokes, and in their modern form constitute the foundation for the numerical modelling of fluid flow. The continuity equation, expressing the law of mass conservation, can be written as [25]:

$$\frac{\partial \rho}{\partial t} + \vec{\nabla}\left(\rho \vec{V}\right) = 0 \tag{1}$$

where ρ is the fluid density, t is time, and V is the velocity vector field. The Navier-Stokes equations represent the conservation of momentum. In the x-direction, they can be expressed as [25]:

$$\frac{\partial (\rho u)}{\partial t} + \vec{\nabla}\left(\rho u \vec{V}\right) = \frac{\partial p}{\partial x} + \frac{\partial t_{xx}}{\partial x} + \frac{\partial t_{xy}}{\partial y} + \frac{\partial t_{zx}}{\partial z} + \rho f_x \tag{2}$$

where p is the static pressure, τ_{ij} are the components of the viscous stress tensor, and f_x is the body force component in the x-direction. Similar relations apply to the y and z directions. The numerical solution of this system of non-linear differential equations requires the introduction of a turbulence model to achieve system closure. Although Direct Numerical Simulation (DNS) resolves all turbulent scales without such modelling, it demands high computational resources. Therefore, this study employs the Reynolds-Averaged Navier-Stokes (RANS) approach, whereby instantaneous velocity and pressure values are decomposed into mean and fluctuating components. This enables the solution of time-averaged flow fields, whilst the effects of turbulence are modelled using empirical relations. The RANS equation for the x-direction is as follows [25]:

$$Q = \frac{1}{2}\left(\|\Omega\|^2 - \|S\|^2\right) \quad (3)$$

where $\bar{u}, \bar{p}, \vec{V}$ are the time-averaged values of velocity, pressure, and velocity vector, τ_{xx}, τ_{yx}, τ_{zx} are the components of the viscous stress for the mean flow, and $\overline{\rho u'u'}$, $\overline{\rho u'v'}$, $\overline{\rho u'w'}$, are the components of the Reynolds stress originating from turbulent fluctuations. To model the turbulent effects, the k-ω SST (Shear Stress Transport) model was employed, as it combines the strengths of both k-ε and k-ω formulations.

The Wilcox k-ω model is used in the near-wall region to provide accurate resolution of the boundary layer, while the formulation transitions to the k-ε model in the free-stream region to improve numerical stability in zones of flow separation and recirculation. The k-ω SST model has proven to be reliable for simulating aerodynamic flows around vehicles and complex geometries, as confirmed by previous studies [22-24]. The model is based on a system of two transport equations describing the distribution of the turbulent kinetic energy (k) and the specific dissipation rate (ω) [26]:

$$\frac{\partial}{\partial t}(\bar{\rho}k) + \frac{\partial}{\partial x_j}\left(\bar{\rho}\bar{u}_j k\right) = \frac{\partial}{\partial x_j}\left[\left(\mu + \sigma_k \mu_t\right)\frac{\partial}{\partial x_j}\right] + \quad (4)$$
$$+ p_k - \beta^* \rho\omega k$$

$$\frac{\partial}{\partial t}(\bar{\rho}\omega) + \frac{\partial}{\partial x_j}\left(\bar{\rho}\bar{u}_j \omega\right) =$$
$$\frac{\partial}{\partial x_j}\left[\left(\mu + \sigma_\omega \mu_t\right)\frac{\partial \omega}{\partial x_j}\right] + 2\left(1 - F_1\right)\bar{\rho}_{\omega 2}\frac{1}{\omega}\frac{\partial k}{\partial x_j}\frac{\partial \omega}{\partial x_j} + \quad (5)$$
$$+ \alpha\frac{\omega}{k}p_k - \beta\bar{\rho}\omega^2$$

where μ is the dynamic viscosity, μ_t the turbulent viscosity, P_k the production term of turbulent kinetic energy, and F_1 a blending function ensuring a smooth transition between the k-ω and k-ε regions. The coefficients α, β, σ_k, σ_ω, and $\sigma_{\omega 2}$ are empirically calibrated constants, determined based on experimental and numerical studies.

The numerical solution of the previously described system of equations was carried out using the STAR-CCM+ software package, employing RANS approach with the k-ω SST turbulence model. Spatial derivatives were discretized using the Finite Volume Method (FVM), which transforms the continuous differential equations into a discrete form through volume integration over the control volumes. For the nonlinear coupling between pressure and velocity, an implicit SIMPLE algorithm (Semi-Implicit Method for Pressure Linked Equations) was used. The discretization of the convective terms was performed with second-order accuracy, providing improved numerical precision in predicting velocity and turbulence gradients in the vicinity of the vehicle body and the barriers. Diffusive terms were solved using central differencing, while an implicit time-stepping scheme with adaptive adjustment of the time step was applied to ensure the stability of the solution.

The convergence criterion in all simulations was defined such that the continuity residual reached the order of magnitude of 10^{-6}. The momentum residuals (x, y, z components) were maintained within the range of 10^{-2} to 10^{-3}, while the residuals for turbulent quantities (specific dissipation rate and turbulent kinetic energy) stabilized at approximately 10^{-3}. In addition, the aerodynamic drag (C_D) and lift (C_L) coefficients were tracked as convergence indicators. A simulation was considered converged only when these integral coefficients reached a stable oscillation, with negligible variations over the final few hundred iterations.

Regarding the quantification of results, the analysis of a vehicle's aerodynamic characteristics commonly relies on dimensionless aerodynamic force and moment coefficients, as well as on the pressure coefficient. Their definitions can be expressed by the following relations:

$$C_D = \frac{D}{\frac{1}{2}\rho A V^2}; C_L = \frac{L}{\frac{1}{2}\rho A V^2}; C_S = \frac{S}{\frac{1}{2}\rho A V^2} \quad (6)$$

$$C_R = \frac{R}{\frac{1}{2}\rho A l V^2}; C_L = \frac{Y}{\frac{1}{2}\rho A l V^2}; C_S = \frac{P}{\frac{1}{2}\rho A l V^2} \quad (7)$$

$$C_p = \frac{p - p_\infty}{\frac{1}{2}\rho V^2} \quad (8)$$

where D denotes the drag force, L the lift force, S the side force, R the roll moment, Y the yaw moment, P the pitch moment, p the local static pressure, p_∞ the free-stream static pressure, ρ the air density, A the vehicle frontal area, l the vehicle wheelbase, and V the free-stream air velocity.

In the analysis of the vehicle's lift force, the distribution of lift between the front (L_F) and rear (L_R) axles is of greater significance to the vehicle's dynamic behaviour than the total lift force (L). Expressions for the individual lift components can be derived from a simplified two-dimensional static analysis (Figure 7) by formulating the equilibrium equations.

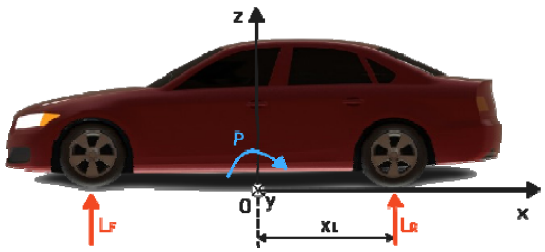

Figure 7. Distribution of loads in vertical plane

The first equation defines the equilibrium of forces along the z - axis, where the sum of vertical forces equals zero:

$$\sum z_i = 0;\ L_F + L_R = L;\ \ L_R = L - L_F \quad (9)$$

The second equation defines the balance of moments around point O, where the sum of moments is equal to 0:

$$\sum M_0 = 0;\ L_F \cdot x_i - L_R \cdot x_i = P; \left(x_i = \frac{l}{2}\right)$$
$$L_R = L_F - \frac{2P}{l} \quad (10)$$

Inserting equation (9) into equation (10) gives the final expressions for lift on the front and rear axle as a function of integral lift (L) and pitching moment (P):

$$L_F = \frac{L}{2} + \frac{P}{l};\ L_R = \frac{L}{2} - \frac{P}{l} \tag{11}$$

Or rather their coefficients:

$$C_{LF} = \frac{L_F}{\frac{1}{2}\rho A V^2};\ C_{LR} = \frac{L_R}{\frac{1}{2}\rho A V^2} \tag{12}$$

For the qualitative analysis of turbulent structures in the wake region, iso-surfaces of Turbulent Kinetic Energy (TKE) and the Q - criterion are commonly used. Turbulent Kinetic Energy is defined as [25]:

$$k = \frac{1}{2}\left(\overline{u'^2} + \overline{v'^2} + \overline{w'^2}\right) \tag{13}$$

where u', v' and w' are the fluctuating velocity compo–nents in the x, y, and z directions, respectively. Essen–tially, this quantity represents the mean kinetic energy per unit mass contained in the turbulent velocity fluctu–ations. It enables the identification of regions with intense turbulent activity, which contribute significantly to the vehicle's total aero-dynamic drag. The Q – cri–terion, on the other hand, is used for vortex core detection and is defined by the expression [25]:

$$Q = \frac{1}{2}\left(\|\Omega\|^2 - \|S\|^2\right) \tag{14}$$

where Ω is the rotation rate tensor (vorticity magnitude squared) and S is the strain rate tensor (deformation magnitude squared). Positive values of Q represent flow regions where rotation dominates over deformation, i.e., the areas where vortex structures are formed.

3. RESULTS AND DISCUSSION

3.1 Validation of CFD model

To confirm the credibility of the numerical model and the reliability of the obtained results, a validation of the CFD model was conducted against experimental data available from wind tunnel measurements performed at the Technical University of Munich (TUM), as pre–sented in [15] and [20]. The numerical setup was desig–ned to replicate the experimental conditions as accura–tely as possible, thereby ensuring that the compa–rison between numerical and experimental results is both relevant and justified.

For the purpose of validation, the DrivAer Notch–back model was employed in a configuration featuring a smooth underbody, side mirrors, smooth tires, and closed wheel rims, scaled at 1:2.5, identical to the expe–rimental setup. The computation-al domain matched the dimensions of the wind tunnel's test section, while the mesh, as well as the initial and boundary conditions, retained the parameters described in the previous section. The base cell size was adjusted to 15 mm at a Reynolds number of 5.2×10^6, corresponding to a free-stream velocity of 42.5 m/s.

Experimentally available data included the drag coefficient (C_D) and the pressure coefficient distribution (C_p) along the vehicle's longitudinal symmetry plane, while other aerodynamic coefficients were not part of the measurements [20]. The simulation predicted a drag coefficient of $C_D = 0.259$, compared with the measured value of $C_D = 0.255$ obtained in the wind tunnel, cor–responding to a deviation of only 1.6 %, thereby confir–ming the satisfactory accuracy of the numerical model.

The pressure coefficient distribution along the upper surface (Figure 8a) and the lower surface (Figure 8b) of the vehicle shows very good agreement between the simulation and the experiment. A minor discrepancy is observed on the upper surface, specifically in the central roof region, where the numerical model predicts slightly lower C_p values. This deviation is attributed to the influence of the vertical mounting strut used in the experiment, which was not included in the CFD simulation.

Consequently, the local flow disturbance it induced is absent in the numerical results. On the lower surface of the vehicle, the agreement is also satisfactory, except for the region between the front wheels, where small differences are evident. These are primarily caused by the presence of the horizontal wheel supports of the experimental vehicle model in the wind tunnel. The obtained results confirm that the developed CFD model is capable of reliably predicting the aerodynamic characteristics of the DrivAer model.

In addition to validating the RANS approach and the k-ω SST turbulence model, a mesh sensitivity analysis was performed on a full-scale model (1:1). This change in scale relative to the initial validation (which used a 1:2.5 scale to match the wind tunnel prototype dimen–sions) required an adjustment of the input parameters. To ensure the same fluid flow characteristics ($Re = 4.87 \times 10^6$ from the experimental wind tunnel testing) [15], the air velocity in the CFD simulation was reduced to 17.7 m/s.

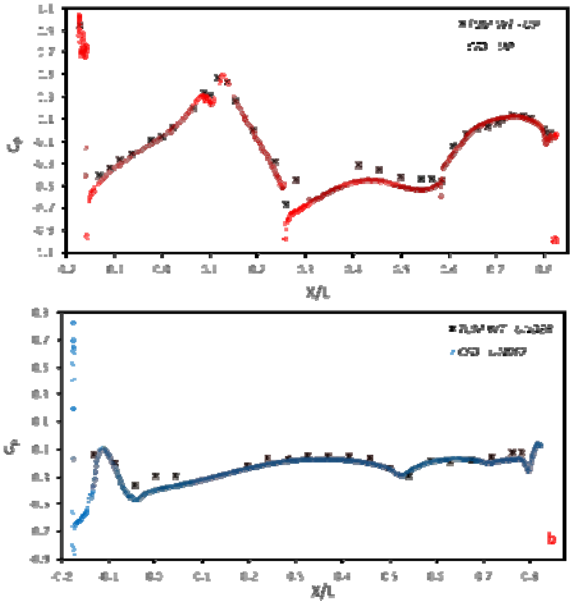

Figure 8. Pressure coefficient in vertical plane of symmetry: a) *upper surface* and b) *bottom surface*

The results of the mesh independence study (Table 2), show that the numerically obtained drag coefficient (C_D) for different mesh densities deviates slightly from the experimental reference value (WT). These differences are minor, with relative error percentages ranging between -1.66 % and 2.30 %.

Based on the analysis of accuracy and required computational time, the 'Fine' mesh was selected as optimal. This mesh has satisfactory accuracy (an error of 2%) with a significantly faster simulation runtime compared to the 'Very Fine' meshes, which is crucial considering that subsequent simulations are conducted within a viaduct environment. To quantify the efficiency of each mesh resolution, a relative computational cost per iteration was calculated and presented in Table 2, where a value of 1.0 corresponds to the 'Coarse' mesh runtime (approximately 0.9 seconds per iteration).

Table 2. Values of drag coefficients for different mesh density

	WT	Very fine	Fine	Medium	Coarse
Cell no.	-	27.5 mil.	17.6 mil.	10.4 mil.	7.2 mil.
C_D	0.246	0.242	0.250	0.242	0.252
Error [%]	-	-1.66	2.01	-1.64	2.30
Rel. cost	-	2.8	1.9	1.1	1.0

3.2 Aerodynamic coefficients: Case analysis 1 to 4

Unlike the simulation used for CFD model validation, all simulations presented in this section of the study were conducted using a full-scale (1:1) vehicle model, with a corresponding Reynolds number of $Re = 1.287 \times 10^7$ (Table 1). This scaling approach based on the Reynolds number is common in aerodynamics, particularly in cases where reduced-scale experimental models are employed. In this manner, it is possible to achieve dynamic similarity between experimental and real flow conditions, or in this case, to numerically reconstruct real driving conditions without the need for additional flow velocity corrections. It is important to ensure that the Reynolds number lies within a range where further increases do not cause significant changes in aerodynamic characteristics.

Previous research [27] has shown that for the DrivAer model, when $Re > 4.87 \times 10^6$, the drag coefficient values no longer exhibit notable variation, thereby justifying the choice of the Reynolds number used in this part of the study. In all cases and scenarios, the same airflow velocity values were maintained, with the longitudinal component set to 42 m/s, while for the second scenario an additional lateral velocity component of 10 m/s was introduced. By scaling the model to 1:1, the same velocity combination was preserved, enabling comparison between the idealized wind tunnel case (Case 1) and more realistic configurations involving a viaduct and windbreaks (Cases 2 - 4).

In the subsequent sections, results are denoted by a combination of numbers (e.g., 1 - 1, 1 - 2), where the first number represents the case number and the second indicates the scenario. Figure 9 illustrates the trend and magnitude of changes in the aerodynamic force and moment coefficients for all four cases and both scenarios, while their numerical values are presented in Table 3. Analysis of the drag coefficient C_D reveals that all values are positive, indicating a drag force acting opposite to the vehicle's direction of motion. In the scenario without a lateral wind component ($\beta = 0°$), the C_D values were very similar across all cases, with the lowest recorded for Case 4 (configuration with a porous windbreak).

This result can be explained by the fact that the porous windbreak reduces flow reflection between the barrier and the vehicle, allowing part of the airflow to pass through the openings, thereby mitigating aerodynamic "flow trapping" and reducing the overall drag. Conversely, in the scenarios with a crosswind component ($\beta = 13.4°$), the C_D values were higher than those at $\beta = 0°$ for all configurations except the porous windbreak. For this configuration, a significant reduction in drag was observed compared to the other cases within the same scenario. This finding indicates that porous windbreaks have a positive influence on the stability of the aerodynamic flow by reducing the vehicle's drag coefficient. The increase in C_D observed in the remaining cases can be attributed to the more complex flow characteristics in the presence of a cross-wind component, which induces asymmetric separation and the formation of larger vortex structures along the vehicle's lateral and rear sections.

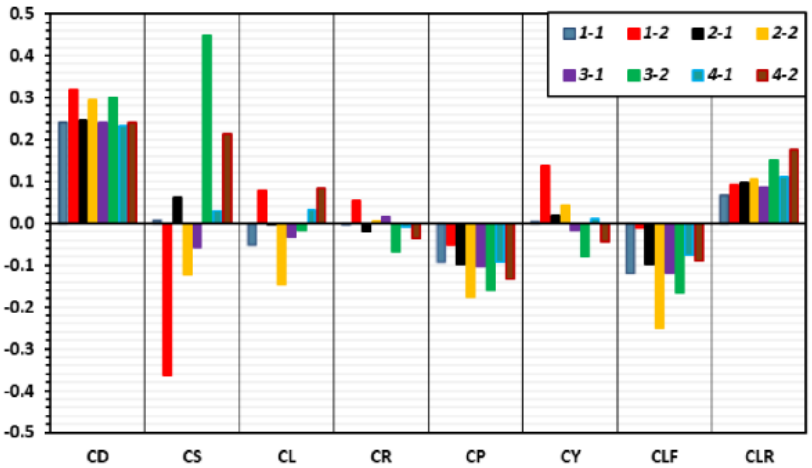

Figure 9. Aerodynamic coefficients for four cases and two scenarios. In the legend, the first number indicates the Case and the second number the Scenario (e.g. Case 1, Scenario 1 is indicated as "1 - 1")

Table 3. Values of aerodynamic coefficients predicted using CFD simulations

Case	β [°]	C_D	C_S	C_L	C_R	C_P	C_Y
1	0	0.240	0.008	-0.052	-0.002	-0.094	0.004
	13.4	0.320	-0.363	0.079	0.054	-0.051	0.138
2	0	0.247	0.062	-0.002	-0.018	-0.098	0.019
	13.4	0.294	-0.123	-0.146	0.005	-0.177	0.042
3	0	0.242	-0.057	-0.034	0.016	-0.103	-0.017
	13.4	0.300	0.448	-0.016	-0.069	-0.159	-0.078
4	0	0.233	0.028	0.033	-0.009	-0.093	0.010
	13.4	0.239	0.214	0.084	-0.036	-0.133	-0.043

Regarding the side force coefficient C_S, a considerably more complex behaviour is observed compared with the drag coefficient. The most prominent feature is the change in the sign of the side force across different cases and scenarios. Specifically, Cases 1 - 1, 2 - 1, 3 - 2, 4 - 1, and 4 - 2 exhibited a positive sign of the force, indicating that the side force acted in the opposite direction to the crosswind W. The remaining cases showed a negative sign, implying that the force acted in the same direction as the lateral wind component. This behaviour results from the pressure difference between the two sides of the vehicle, which can be clearly seen in Figure 10, showing the surface pressure coefficient (C_p) distribution for Cases 1 - 2 and 4 - 2. In particular, in Case 1 - 2, the windward side of the vehicle (the side directly exposed to the incoming wind) is dominated by high-pressure regions, whereas the leeward side exhibits significantly lower pressure. This pressure difference generates an integrated side force that tends to "push" the vehicle from the region of higher pressure towards the region of lower pressure. The largest negative value of the side-force coefficient was recorded for Case 1 - 2, which is expected, since in this configuration the vehicle is fully exposed to the crosswind without any shielding barriers or fences. Conversely, the highest positive C_S value occurs in Case 3 - 2, which employed an impermeable windbreak (solid windbreaks). In this configuration, interference arises between the airflow impinging on the vehicle's windward side and the reflected flow forming between the vehicle and the barrier. As a result, a pronounced recirculation zone develops in this region, creating a suction effect that tends to draw the vehicle towards the barrier. This is a particularly important observation in understanding aerodynamic stability under crosswind conditions, as it indicates that impermeable windbreaks can, under certain circumstances, generate undesirable aerodynamic interactions that may adversely affect the vehicle's lateral stability and handling performance.

When analysing the integral lift coefficient (C_L), it can be observed that its sign varies depending on the configuration and flow conditions. Specifically, for Cases 1 - 2, 4 - 1, and 4 - 2, C_L has a positive sign, whereas it is negative for the remaining cases. From an aerodynamic standpoint, a negative lift value has a beneficial effect on vehicle stability, as it contributes to "pressing" the vehicle towards the ground, thereby enhancing tire adhesion and improving stability during motion. Conversely, a positive C_L indicates a tendency for upward lift, which may adversely affect vehicle stability. The computed aerodynamic lift forces are on the order of ±200N, which is substantially lower than the typical weight of a vehicle. Although the integral lift provides a general indication of vertical aerodynamic forces, it is not sufficient for a detailed assessment of the vehicle's dynamic behaviour. More informative are the partial lift coefficients at the front (C_{LF}) and rear (C_{LR}) axles, as these directly influence the pressure distribution and the vehicle's pitching moment. Figure 9 presents the values of these coefficients for all analysed cases and scenarios. It is evident that all C_{LF} values are negative, while C_{LR} values are positive, which aligns with expectations after observing the pressure coefficient distribution on the vehicle surface.

From a physical perspective, a negative C_{LF} indicates a downward force (downforce) acting on the vehicle's front section. This phenomenon is highly favourable in terms of stability, as it presses the vehicle towards the road and reduces the possibility of the vehicle's movement deviating from the desired trajectory. The lowest C_{LF} absolute value was recorded for Case 1 - 2, as expected, since this case involves an airflow that includes a side wind component, and the vehicle is directly exposed to that wind without any surrounding protection. The highest C_{LF} absolute value was found for Case 2 - 2, where the guard-rail generated a complex interaction between the incoming and through-flowing air, leading to a local decrease in lift on the vehicle's front section. In contrast, C_{LR} exhibits an opposite trend, where a positive lift force sign negatively affects vehicle stability during driving and attempts to "lift" the vehicle off the road.

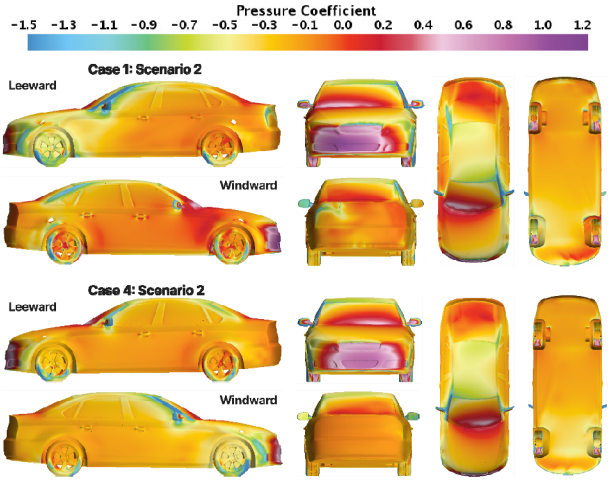

Figure 10. Pressure coefficient distribution on vehicle surface for Case 1 – 2 and 4 – 2

The lowest lift coefficient (C_{LR}) was observed in Case 1 - 1, where the vehicle is exposed to a longitudinal airflow component and has no surrounding protection. Conversely, the highest C_{LR} value was recorded for Case 4 – 2, where the porous windshield caused complex airflow and vortex structures around the rear section of the vehicle and behind the vehicle.

With respect to the rolling-moment coefficient (C_R), a clear trend consistent with the behaviour of the side force was observed. The largest (in absolute terms) negative value was recorded for Case 3 - 2, where the roll-moment vector has the same direction but opposite sense to the aerodynamic drag force vector. Such a moment orientation indicates an increased tendency of

the vehicle to rotate in the direction of the acting side force, which may adversely affect lateral stability. Conversely, the largest (in absolute terms) positive C_R value was observed for Case 1 - 2, where the roll-moment vector acts oppo-site to the vehicle's direction of motion. In the remaining cases, the C_R values are smaller. However, their sign and magnitude remain correlated with changes in the direction of the side force S, confirming the consistency of the flow and pressure distribution around the vehicle.

The pitching-moment coefficient (C_P) exhibits consistently negative values for all analysed airflow cases around the vehicle. By definition in the CFD setup, the pitching moment (P) is defined along the local y - axis of the vehicle, which passes through the midpoint of the wheel-base, while the reference point of the moment is positioned at ground level (Figure 7). The negative C_P values result from the combined influence of pressures on the upper and lower surfaces of the vehicle body. This can be confirmed through the analysis of the pressure coefficient (C_p) distribution in the vehicle's longitudinal symmetry plane - on the upper (Figure 11a) and lower (Figure 11b) surfaces.

On the upper surface of the vehicle, negative C_p values dominate along almost the entire body, except in the stagnation zone at the front section, the transition between the bonnet and the windscreen, and the transition from the rear windscreen to the boot lid. These low-pressure regions result from the acceleration of airflow over the curved vehicle surface, generating an upward lift force.

On the lower side of the vehicle, particularly beneath the front bumper and between the wheels, negative C_p values are also present, but they act in the opposite direction, i.e., downwards, contributing to the formation of a downforce effect. As the flow progresses towards the rear section of the underbody, a slight increase in C_p is observed, although it remains within the negative domain. This confirms that the airflow beneath the vehicle is faster than the surrounding flow, corresponding to a lower static pressure. The combined effect of the pressure distribution on the upper and lower surfaces results in a pitching moment that presses the vehicle's front section towards the ground, while the rear section tends to experience a slight lifting effect. In other words, the contribution of the forces producing a "nose-down" effect outweighs that of the forces generating a "nose-up" moment, thereby explaining the negative C_P values. Regarding the position of the centre of pressure (CoP), in all cases it is located behind the centre of gravity (CoG). Such a CoP position indicates that the aerodynamic forces act in a way that causes the vehicle to rotate about the CoG in a direction that lowers the front end and presses the vehicle against the ground, thereby enhancing its longitudinal stability.

The yaw-moment coefficient (C_Y) plays a significant role in the analysis of the aerodynamic stability of passenger vehicles under crosswind conditions. Unlike heavy goods vehicles, for which the rolling moment is dominant due to their higher centre of gravity, the yaw moment is more critical in passenger cars. It describes rotation about the vehicle's vertical axis, which directly affects lateral stability and handling behaviour. The vertical axis (the z - axis of the local coordinate system) passes through the reference point shown in Figure 7, and the yaw moment is defined such that its vector has the same direction as this axis. The results indicate that negative C_Y values were obtained for Cases 3 - 1, 3 - 2, and 4 - 2, meaning that the aerodynamic moment acts to rotate the vehicle such that the front end turns towards the windbreak, while the rear section moves away from it.

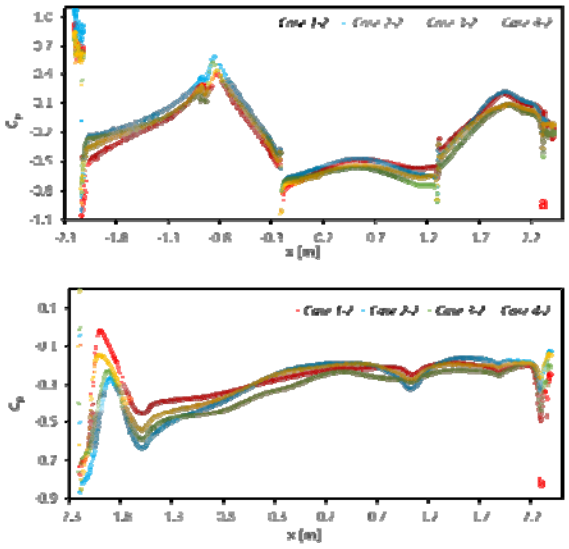

Figure 11. Pressure coefficient distribution on vehicle surface in vertical plane: a) *upper surface* and b) *bottom surface (all cases in scenario 2)*

Conversely, positive C_Y values for the remaining cases indicate the opposite effect, the vehicle's front end rotates away from the oncoming wind, and the rear section turns towards it. It is interesting to note that even in scenarios without a lateral wind component ($\beta = 0°$), a pronounced interference effect occurs between the vehicle and the surrounding infrastructure elements, particularly in the presence of protective guardrails and impermeable windbreaks. While in Case 1 (the free-flow condition) the C_Y value is nearly zero, Cases 2, 3, and 4 show a noticeable increase in the yaw moment, indicating that even under nominally longitudinal airflow conditions, asymmetric flow structures develop around the vehicle due to reflection and vortex formation between the vehicle and the barriers (Figure 12).

The introduction of a crosswind component ($\beta = 13.4°$) reveals a beneficial effect from the protective guardrails and the porous wind-break. This effect is characterized by a decrease in the absolute value of C_Y, which reduces the vehicle's tendency to rotate and thereby improves its overall aerodynamic stability. Based on the analysis of all aerodynamic coefficients, it can be concluded that the presence of guardrails and windbreaks has a pronounced influence on pressure distribution and the aerodynamic behaviour of the vehicle. The conventional guardrails, represented by the New Jersey barrier type, proved effective in mitigating the effects of crosswinds in the near-ground region, thereby slightly reducing both the side force and the rolling moment. However, its influence on the integral drag coefficient was found to be insignificant, indicating that it neither decreases nor increases drag to an extent that would noticeably alter the overall aerodynamic

characteristics. In contrast, impermeable windbreaks exhibited a more pronounced flow reflection effect between the vehicle and the barrier, which can lead to increased side forces and moments, particularly yawing and rolling moments at higher crosswind velocities.

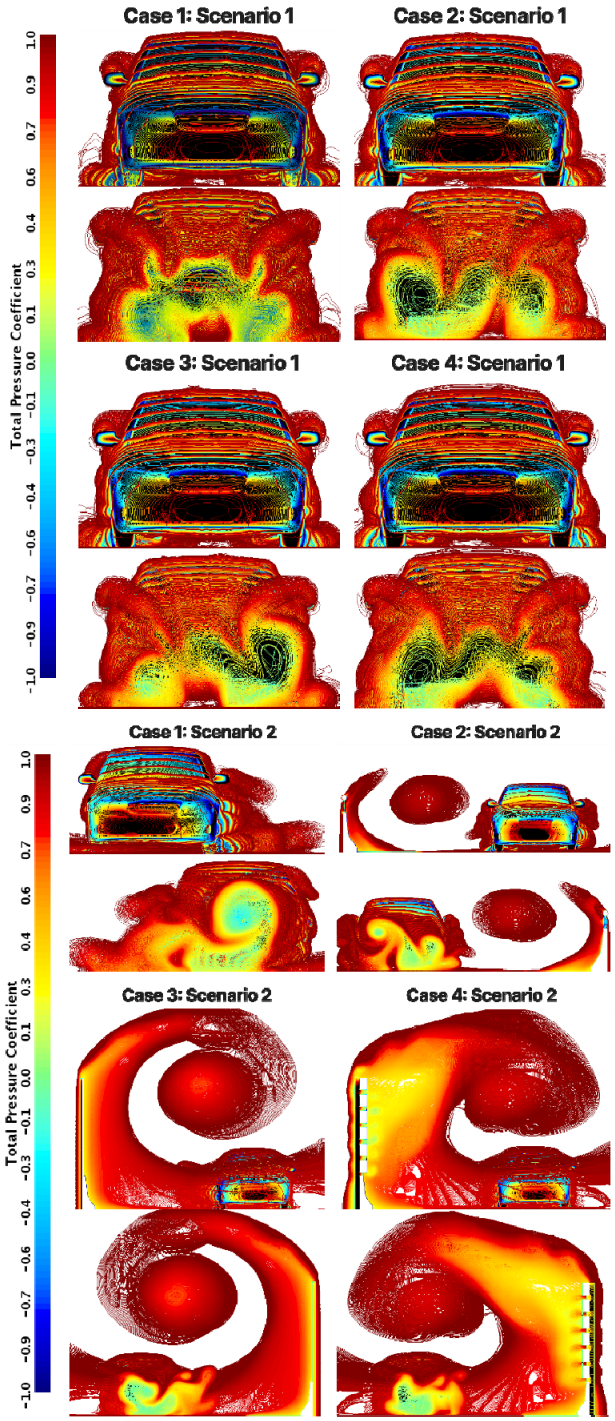

Figure 12. Contour Plot of Pressure Coefficient around vehicle and bridge surface

Conversely, porous windbreaks produced the most favourable results, as they allow partial airflow through their openings, reducing flow reflection and turbulence in the region between the vehicle and the protective structure. Consequently, they simultaneously reduce the drag and side-force coefficients, thus enhancing vehicle stability under crosswind conditions. In summary, porous windbreaks can be regarded as the optimal solution in terms of overall aerodynamic stability and drag reduction. The conventional guardrails provide sufficient aerodynamic protection for passenger vehicles under most realistic driving conditions, especially where extreme crosswind effects are not expected. The installation of impermeable windbreaks for passenger cars is not justified, as they do not yield significant improvements compared with standard barriers. However, their application may be more beneficial for heavy goods vehicles, where the larger lateral surfaces and higher centre of gravity result in more pronounced rolling moments and side forces.

3.3 Flow visualization and vortex structures

The visualization of the flow field around the vehicle, particularly through the use of the Q - criterion, provides valuable insight into the formation, evolution, and spatial distribution of complex vortex structures in the vehicle's wake region. The Q - criterion is one of the most widely employed methods in turbulent flow analysis, as it enables the identification of regions where the rotational components of the fluid velocity dominate over the strain-rate components. In this study, Q - criterion iso-surfaces at a value of $Q = 400\ s^{-2}$ were visualized and color-coded according to the local velocity magnitude (m/s).

Figure 13a presents the results for all four configurations (Cases 1 - 4) under Scenario 1 ($\beta = 0°$). For all cases, characteristic vortex structures can be observed forming in the vehicle's rear region, predominantly around the C - pillar zone and the upper roof edges. This observed flow behaviour is consistent with the expected aerodynamics of a notchback-type vehicle. In Case 1, a broad and highly turbulent wake region is clearly visible behind the vehicle, where paired vortices extend along the longitudinal axis and retain high kinetic energy. In Cases 2, 3, and 4, the same basic flow pattern is preserved. However, significant differences can be noted in the spatial development and intensity of the vortex structures. The vortices appear more pronounced and persist over a longer distance, while the velocity distribution within the vortical cores remains within a similar range as in the first case. Nonetheless, the overall vortex structure extends further in both vertical and lateral directions.

In Figure 13b, the results for all analysed cases under Scenario 2 ($\beta = 13.4°$) are presented. In comparison with Scenario 1, the presence of a crosswind component considerably alters the distribution and intensity of the vortical structures in the wake region behind the vehicle, most notably affecting the shape and orientation of the wake zone. In Cases 1 and 2 vortices forming behind the A - pillars, with more pronounced asymmetric behaviour can now be observed.

On the wind-ward side of the vehicle, more compact vortices with higher velocity intensity are generated, whereas on the leeward side, the vortices are longer and more diffused, indicating stronger flow separation and the emergence of secondary vortices. Localized flow acceleration can be noticed along parts of the roof and rear pillars, resulting from the interaction between the main stream and the crosswind component.

Case 3 (Scenario 2) exhibits a distinctly different pattern of vortex formation, dominated by a high-

velocity structure extending above the vehicle and influencing the downstream flow. This feature originates from flow separation at the upper edge of the solid windbreak, forming an elongated vortical filament that stretches along the viaduct segment. The interaction between the flow over the vehicle and that along the barrier generates a recirculation zone and regions of accelerated airflow adjacent to the barrier surface. In Case 4, where a porous windbreak is employed, the flow pattern largely returns to that observed in Scenario 1, without the pronounced crosswind-induced asymmetry. This demonstrates that barrier porosity allows for partial airflow transmission, effectively reducing flow reflection and mitigating the development of strong vortical structures within the wake region.

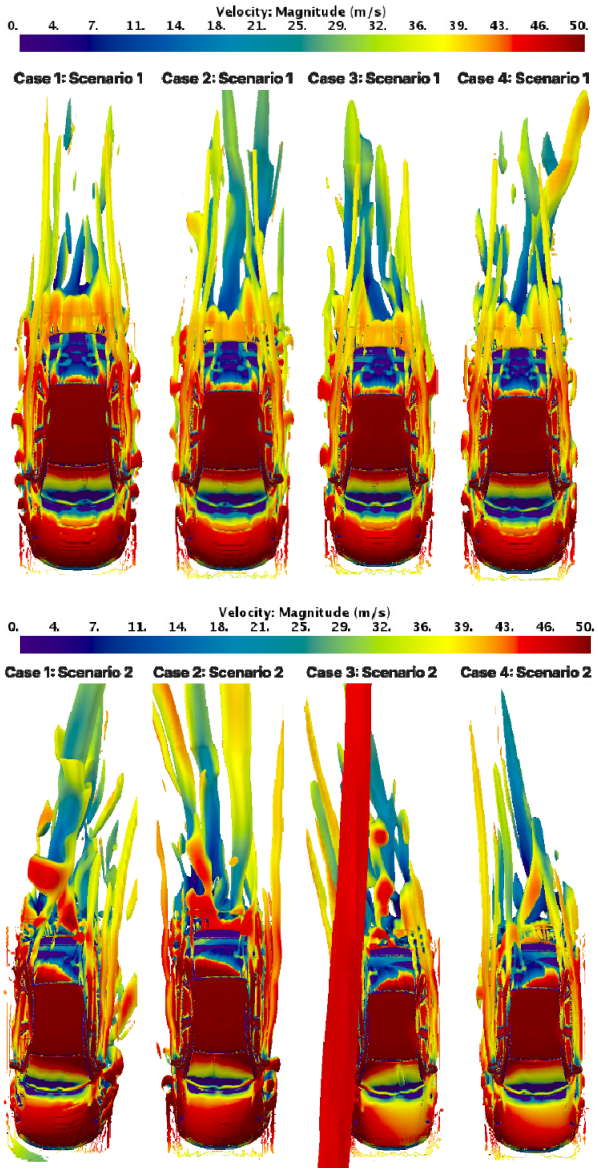

Figure 13. Q - criterion iso-surfaces (isovalue = 400 1/s²) coloured by flow velocity (m/s) for all cases: a) Case 1 - 4 under Scenario 1 (β = 0°), b) Case 1 - 4 under Scenario 2 (β = 13.4°)

Figure 14 presents iso-surfaces of turbulent kinetic energy (TKE) at an isovalue of 15 J/kg, colored according to the local flow velocity magnitude. Turbulent kinetic energy quantifies the energy contained within turbulent fluctuations of the fluid, providing insight into the intensity and spatial distribution of turbulent structures within the flow field. High TKE values indicate the presence of strong vortex motion, increased energy dissipation, and enhanced fluid mixing within the wake region.

The results shown in Figure 14a, corresponding to all four cases under Scenario 1 ($\beta = 0°$), clearly illustrate variations in the shape and extent of the turbulent wake behind the vehicle. Case 2 exhibits the widest and most intense TKE region, with pronounced low-velocity zones extending far downstream, indicating an extensive vortex region and a high level of turbulence. Case 1 demonstrates a narrower turbulent energy wake, whereas in Case 3, the wake be-comes even more localized. Case 4, featuring the porous windbreak, presents the smallest and least intense TKE zone, confirming the stabilizing influence of partial flow permeability.

Figure 14b presents the simulation results for all cases within Scenario 2 ($\beta = 13.4°$). In Case 1, the turbulent kinetic energy (TKE) wake behind the vehicle is broad and spatially developed, featuring an asymmetrical shape that mildly rotates towards the vehicle's leeward side (driver's side). Low-velocity regions dominate the rear zone of the vehicle, while high velocities are concentrated along the side surface of the windward side, particularly around the driver's door area, indicating augmented vorticity. In Case 2, where the vehicle is situated on a viaduct with a guardrail, the shape and intensity of the turbulent wake change significantly.

The wake becomes more pronounced and spatially wider, with higher velocities observed on the leeward side and a longer retention of the elevated intensity zone. Concurrently, the presence of the barrier partially influences the redirection of the flow above and alongside the vehicle, while simultaneously stabilizing the flow in the lower zone. In Case 3, the turbulent flow pattern changes completely compared to the previous cases. Due to the reflection of the airflow between the vehicle and the solid barrier, a highly asymmetrical wake occurs, featuring higher velocities and increased TKE values in the vicinity of the windward side. The flow is redirected along the barrier, creating a prominent recirculation zone that extends along the rear of the vehicle and is directed upwards. In Case 4, owing to the barrier's porosity, a portion of the air passes through the windbreak openings, thereby reducing reflection and mitigating the recirculation between the vehicle and the protective structure. This results in a significantly narrower and more stable turbulent kinetic energy wake, with the lowest velocity values compared to the other cases.

Additional insight into flow dynamics and the formation of vortex structures can be gained by analysing the streamlines and velocity field in the y - z plane of the vehicle's local coordinate system. This plane allows for the visualization of the interaction between the air-flow, the bridge surface, and the lateral elements, as well as the genesis and development of vortices in the space between the vehicle and the guardrail. Figure 15a illustrates Cases 2, 3, and 4 within Scenario 1.

In Case 2, a mild interaction between the vehicle and the airflow is observable, with the streamlines predominantly following the shape of the vehicle without signi–

ficant separation. For Case 3, featuring an impermeable windbreak, the flow is relatively uniform and calm, whereas in Case 4, interaction with the impermeable barrier causes a slight deviation of the flow from the vehicle's side surface and its redirection upwards, indi–cating increased air uplift in the zone between the vehicle and the barrier.

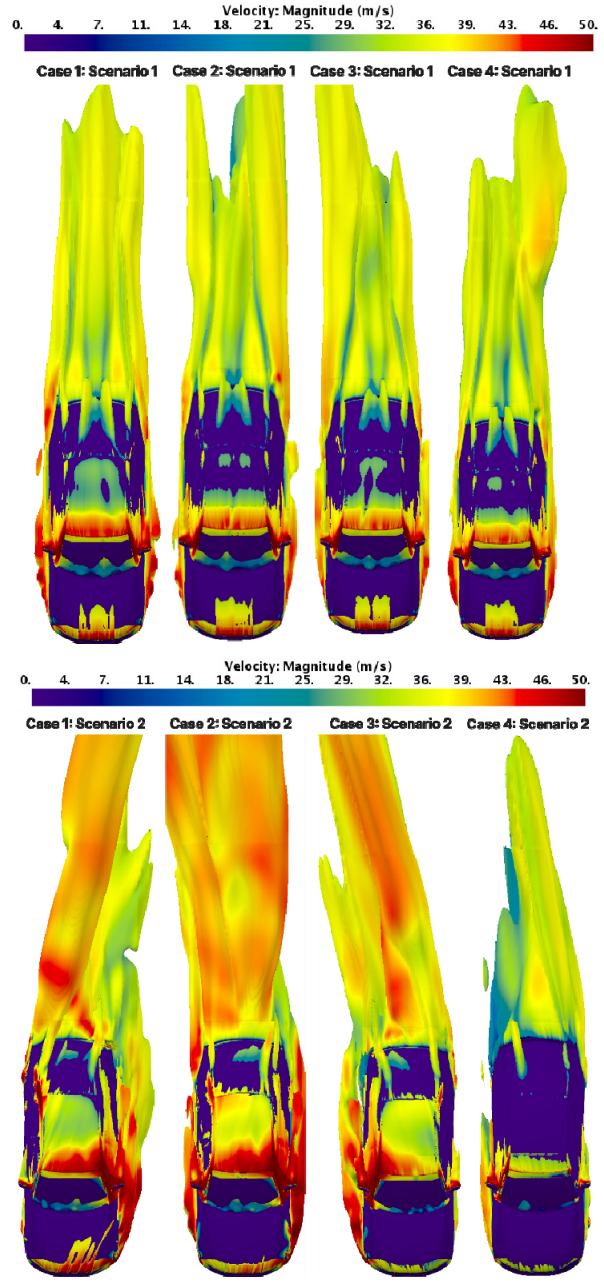

Figure 14. Iso-surface of turbulent kinetic energy (TKE = 15 J/kg) coloured by flow velocity intensity (m/s) for all cases: a) Case 1 - 4 under Scenario 1 (β = 0°); b) Case 1 - 4 under Scenario 2 (β = 13.4°)

In Scenario 2, the situation is more complex due to the influence of the lateral wind component, leading to the formation of closed vortex structures between the vehicle and the side obstacles. In Case 2, the vortex is nearly symmetrical and positioned precisely between the vehicle and the protective railing, indicating a stable flow. In Case 3, the vortex structure becomes more pronounced where the vortex remains symmetrical but features a wider radius and a centre shifted slightly below the top of the windbreak vertically, while horizontally it is located approximately in the zone of the right-hand mirror (windward side).

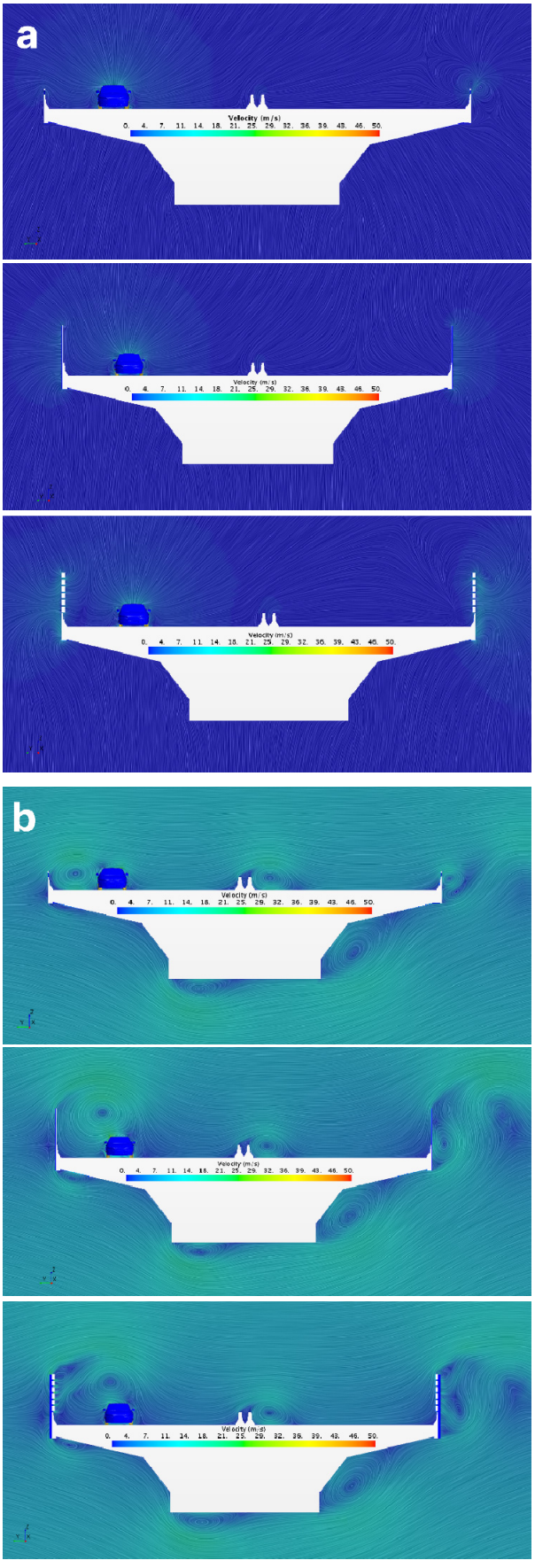

Figure 15. Velocity field and streamlines in the y - z plane of the local coordinate system for: a) cases 2 - 4 in scenario 1 and b) cases 2 - 4 in scenario 2

In Case 4, the flow field exhibits the most complex structure, featuring two separate, asymmetrical vortices of different dimensions. The smaller vortex forms near the top of the windbreak, while the larger one is situated slightly above the vehicle's roof, at a lower height compared to the vortex in Case 3. This configuration suggests a more intricate interaction process between the main flow and the secondary currents generated by the partial passage of air through the porous windbreak, which may warrant further detailed investigation.

4. CONCLUSIONS

The conducted CFD analyses provided a detailed insight into the aerodynamic behaviour of a passenger vehicle (DrivAer model in the Notchback configuration) when travelling over a viaduct in different protective element configurations and under various airflow directions. The results confirmed that the geometry and permeability of the barriers have a significant impact on pressure distribution, the occurrence of turbulent zones, and the overall aerody–namic forces and moments acting on the vehicle.

The validation of the CFD model demonstrated very good agreement with the experimental results from the TUM wind tunnel, with a difference in the drag coeffi–cient amounting to only 1.6 %. This confirms that the mo–del accurately enough describes the aerodynamic pheno–mena of the vehicle and can be reliably used for the analy–sis of more complex bridge - vehicle interaction cases.

The results of the four analysed cases show that the presence of protective elements on the viaduct had a pronounced impact on all aerodynamic coefficients. For Scenario 1 (without the presence of a side wind com–ponent), the drag coefficient (C_D) did not change signi–ficantly. The lowest C_D was recorded in the case with the permeable windbreak (Case 4), while the highest was recorded in Case 2 (with the guardrail). The side force coefficient (C_S) was the lowest in absolute value for Case 1, and the highest for Case 2. The integral lift coefficient (C_L) was the lowest in absolute value for Case 2, while it was the highest for Case 1.

On the other hand, for Scenario 2 (with a side wind component), the situation changes. The highest C_D value was recorded for the reference Case 1, and the lowest for Case 4, which con-firms the positive impact of the permeable windbreak. The side force coefficient was the lowest in absolute value for Case 2, while it was the highest for Case 3. This indicates that for passenger ve–hicles, a protective barrier in the form of "New Jersey" blocks yields good results in terms of reducing wind impact, whereas the issue with impermeable windbreak is highlighted due to the effects of air flow reflection between the vehicle and the wind-screen. The integral lift coefficient was the lowest in ab-solute value for Case 3, while it was the highest for Case 2.

The analysis of the velocity field, the Q - criterion, and the TKE iso-surfaces confirmed these conclusions. In cases (Case 1 - 3), the wake zone was broad and tur–bulent, with pronounced vorticity and high values of turbulent kinetic energy. For the porous windbreak (Case 4), the turbulent flow wake was the narrowest, with the lowest intensity of turbulence, which directly indicates the efficiency of such a solution.

Overall, the results show that the application of porous windbreaks has a positive effect on the aero–dynamic behaviour of passenger vehicles on viaducts, particularly during side wind gusts. Their ability to reduce pressure and turbulence, with minimal impact on resistance, makes them more effective than imper–meable barriers. Given that passenger vehicles are lower and more aerodynamically stable than heavy goods vehicles (HGVs), the installation of a standard guard–rails is usually sufficient, while in areas with strong crosswinds, the addition of porous windbreaks could significantly im-prove vehicle safety and stability. Further research into the influence of windbreaks on vehicle aerodynamics will focus on analysing the impact of the size of the air passages, i.e., the porosity of the windbreaks, for different geometries.

Beyond the immediate aerodynamic findings, this study provides a practical framework for civil and traffic engineers to optimize infrastructure design on wind-exposed sections. The scientific merit of providing quantified aerodynamic coefficients for such complex scenarios directly contributes to the development of more accurate safety protocols for different vehicle types. Also, these results serve as a reliable basis for future multi-body dynamic simulations aimed at predic–ting and preventing vehicle instability or rollover acci–dents in real-world operating conditions.

ACKNOWLEDGMENT

This research received no specific grant from any fun–ding agency in the public, commercial, or not-for-profit sectors.

REFERENCES

[1] Hucho. WH, editor: *Aerodynamics of road vehicles: from fluid me-chanics to vehicle engineering*. 2nd edn. Elsevier, England, 2013.

[2] Trobradović, M., Šehović, J., Pervan, N., Blažević, A., Lulić, H., Hadžiabdić, V., Muminović, A.J., "Assessment of the Impact of Vehicle Electri–fication on the Increase in Total Electrical Energy Consumption in Bosnia and Herzegovina," *World Electric Vehicle* Journal, Vol. 16, no.7, p.362, 2025.

[3] Jiao, D., Zhou, H., Huang, T., Zhang, W., "Nume–rical Study on Aerodynamic Noise Reduction in Passenger Car with Fender Shape Optimization," *Symmetry*, vol. 16, no. 6, p. 651, 2024.

[4] Trakić, A., Trobradović, M., Torlak, M., "The Impact of Crosswind Induced Aerodynamics Loads on Vehicle Stability," International Symposium and the 16th Days of BHAAAS. In: *Ademović N, Akšamija Z, Karabegović A. (eds) Advanced Tech–nologies, Systems, and Applications X. IAT*, Sarajevo, 19 – 22 June 2025.

[5] Lawson, A., Dominy, R., Sims-Williams, D., Mears, P., "A Comparison Between On-Road and Wind Tunnel Surface Pressure Measurements on a Mid-Sized Hatchback," *SAE Technical Paper* 2007-01-0898, 2007.

[6] Sterling, M. et al., "A comparison of different met–hods to evaluate the wind induced forces on a high

sided lorry," *Journal of Wind Engineering and Industrial Aerodynamics*, vol. 98, no. 1, pp.10-20, 2010.

[7] Zhang, M., Zhang, J., Long, J., Li, Y., Zou, Y., Yin, D., "CFD Numerical simulation of wind field and vehicle aerodynamic characteristics on truss bridge deck under crosswind," *KSCE Journal of Civil Engineering*, vol. 26, no. 12, pp. 5146-59, 2022.

[8] Wang, L., Chen, X., Chen, H., "Research on wind barrier of canyon bridge-tunnel junction based on wind characteristics," *Advances in Structural Engineering*, vol. 24, no. 5, pp. 870-83, 2021.

[9] Zhang, J., Zhang, M., Li, Y., Jiang, F., Wu, L., Guo, D., "Comparison of wind characteristics in different directions of deep-cut gorges based on field measurements," *Journal of Wind Engineering and Industrial Aerodynamics*, vol. 212, p. 104595, 2021.

[10] Cheli, F., Ripamonti, F., Sabbioni, E., Tomasini, G.I., "Wind tunnel tests on heavy road vehicles: Cross wind induced loads - Part 2," *Journal of Wind Engineering and Industrial Aerodynamics,* vol. 99, no. 10, pp. 1011-24, 2011.

[11] Salati, L., Schito, P., Rocchi, D., Sabbioni, E., "Aerodynamic study on a heavy truck passing by a bridge pylon under crosswinds using CFD," *Journal of Bridge Engineering*, vol. 23, no. 9, p. 04018065, 2018.

[12] Guo, J., Tang, H., Li, Y., Wang, Z., "Effects of guardrails on wind environment for vehicles and aerodynamic stability for bridges with box girders," *Advances in Structural Engineering*, vol. 24, no. 3, pp. 453-69, 2021.

[13] Ni, Z., Zhang, C., Zhang, L., Liu, L., "Effects of the wide-body suspension bridge auxiliary structure on flutter characteristics by CFD," *Vibro-engineering Procedia*, vol. 28, pp. 223-9, 2019.

[14] He, X., Xue, F., Zou, Y., Chen, S., Han, Y., Du, B., Xu, X., Ma, B., "Wind tunnel tests on the aerodynamic characteristics of vehicles on highway bridges," *Advances in Structural Engineering*, vol. 23, no. 13, pp. 2882-97, 2020.

[15] Heft, A., Indinger, T., and Adams, N., "Introduction of a New Realistic Generic Car Model for Aerodynamic Investigations," *SAE Technical Paper* 2012-01-0168, 2012.

[16] Ahmed, S., Ramm, G., Faltin, G., "Some Salient Features Of The Time-Averaged Ground Vehicle Wake," *SAE Technical Paper* 840300, 1984.

[17] Tarakka, R., Salam, N., Jalaluddin, J., Ihsan, M., "Effect of blowing flow control and front geometry towards the reduction of aerodynamic drag on vehicle models," *FME Transactions*, vol. 47, no. 3, pp. 552-9, 2019.

[18] Ashton, N., Van, Noordt, W., "Overview and summary of the first automotive CFD prediction workshop: DrivAer model," *SAE International Journal of Commercial Vehicles*, vol. 16, no. 1, pp. 61-85, 2023.

[19] Bearman, P., "Some Observations on Road Vehicle Wakes," *SAE Technical Paper* 840301, 1984.

[20] Peichl, M., Mack, S., Indinger, T., Decker, F., "Numerical investigation of the flow around a generic car using dynamic mode decomposition," In *Fluids Engineering Division Summer Meeting 2014 Aug 3* (Vol. 46230, p. V01CT17A002).

[21] Watkins, S. et al. "Turbulence experienced by moving vehicles. Part I. Introduction and turbulence intensity," *Journal of Wind Engineering and Industrial Aerodynamics*, vol. 57, no. 1, pp. 1-7, 1995.

[22] Simmonds, N. et al., "Complete Body Aerodynamic Study of three Vehicles," *SAE Technical Paper* 2017-01-1529, 2017.

[23] Fu, C., Bounds, C., Uddin, M., Selent, C., "Fine Tuning the SST k − ω Turbulence Model Closure Coefficients for Improved NASCAR Cup Race-car Aerodynamic Predictions," *SAE Int. J. Adv. & Curr. Prac. in Mobility*, vol. 1, no. 3, pp. 1226-1232, 2019.

[24] Lacombe, F., Pelletier, D., Garon, A., "Compatible wall functions and adaptive remeshing for the k-omega SST model," In: *AIAA Scitech 2019 Forum* vol. 1, p. 2329, 2019.

[25] Tennekes, H., Lumley, J.L., *A first course in turbulence*, MIT Press Cambridge, Massachusetts, and London, England, 1972.

[26] Menter, F.R., "Two-equation eddy-viscosity turbulence models for engineering applications," *AIAA journal*, vol. 32, no. 8, pp. 1598-605, 1994.

[27] Heft, A. et al., "Experimental and numerical investigation of the DrivAer model," American Society of Mechanical Engineers, *In Fluids engineering division summer meeting 2012*, 44755:41-51, 2012.

NOMENCLATURE

β	Yaw angle
C_D	Drag force coefficient
C_L	Lift force coefficient
C_{LF}	Lift force coefficient on front axle
C_{LR}	Lift force coefficient on rear axle
C_S	Side force coefficient
C_P	Pitch moment coefficient
C_Y	Yaw moment coefficient
C_R	Rolling moment coefficient
Re	Reynolds number
A	Frontal Area
l_{ref}	Reference length
l	Vehicle wheelbase
U	Air velocity in x – direction
W	Wind speed in y – direction
V	Relative wind speed

УТИЦАЈ ВИЈАДУКТА И ВЈЕТРОБРАНСКИХ ОГРАДА НА АЕРОДИНАМИКУ ВОЗИЛА: CFD СТУДИЈА

А. Тракић, М. Тобрадовић, Ц. Бибић, Е. Џаферовић

Ова студија представља нумеричку симулацију струјања ваздуха око путничког возила (DrivAer

модел у Notchback конфигурацији) током кретања преко вијадукта, са циљем анализе утицаја заштитних ограда на аеродинамичке карактеристике возила. CFD симулације су спроведене у програму STAR-CCM+ коришћењем RANS приступа у комбинацији са k-ω SST моделом турбуленције. Анализиране су четири геометријске конфигурације: слободно струјање без заштите, вијадукт са заштитном оградом, вијадукт са непорозним вјетробраном и вијадукт са порозним вјетробраном за заштиту од вјетра. Свака конфигурација је симулирана у два сценарија струјања, са и без компоненте бочног вјетра. CFD модел је валидиран поређењем са експерименталним подацима добијеним у аеротунелу Техничког универзитета у Минхену (TUM), при чему је показано задовољавајуће поклапање коефицијената отпора и притиска. Резултати указују на то да непорозни вјетробрани повећавају бочне силе и моменте ваљања, док порозни вјетробрани значајно смањују ефекте турбуленције и побољшавају аеродинамичку стабилност. Анализа поља Q-критеријума и турбулентне кинетичке енергије потврђује да порозна баријера сужава зону трага и смањује вртложне структуре иза возила. Додатно је утврђено да код путничких возила добро пројектована заштитна ограда може постићи упоредиве или чак боље ефекте у односу на комплексне вјетробранске структуре у погледу оптимизације аеродинамичких оптерећења на возило.